International Journal of Hydrogen Energy 148 (2025) 149770

Contents lists available at ScienceDirect

International Journal of Hydrogen Energy

journal homepage: www.elsevier.com/locate/he

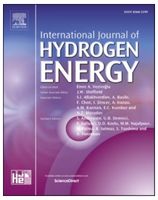

Joule-heated PdFe alloys with phase-dependent electronic structures for high-efficiency oxygen reduction

Dandan Jiang, Danyang Wu [*], Yu Wang, Yongze Cao, Xizhen Zhang, Baojiu Chen [**]

School of Science, Dalian Maritime University, Dalian, 116026, China

A R T I C L E I N F O

Handling Editor: Søren Juhl Andreasen

Keywords:
Pd-based alloys
Joule-heating synthesis
Cubic-phase alloy nanoparticles
Oxygen reduction reaction

A B S T R A C T

The design of Pd-based alloys with tailored electronic structures and stable architectures is crucial for enhancing catalytic properties. Here, we present a rapid Joule heating strategy for fabricating a palladium-iron (PdFe) alloy anchored on nitrogen-doped carbon (NC–FePd) featuring exceptional performance and durability. By combining ultrafast phase formation and quenching, the NC-FePd system achieves uniform dispersion of cubic-phase $FePd_3$ nanoparticles with minimized agglomeration. X-ray diffraction and XPS analyses reveal lattice expansion planes and electron transfer between Pd and Fe, which lowers the d-band center of Pd, thereby weakening the Pd–O binding energy. In alkaline media, NC-FePd achieves an exceptional half-wave potential (0.84 V vs. RHE), showing a clear advantage over commercial Pt/C (0.82 V vs. RHE), coupled with elevated limiting current density (6.01 mA cm^{-2}) and the diminished Tafel slope (53.73 mV dec^{-1}). This work sheds light on the synergy between rapid Joule-heating synthesis and Fe–Pd electronic modulation for designing durable alloy catalysts.

1. Introduction

Proton exchange membrane fuel cells (PEMFC) represent crucial devices for sustainable energy conversion, but their commercialization is still hampered by sluggish oxygen reduction reaction (ORR) kinetics and high overpotential [1–4]. Although platinum-based catalysts dominate ORR catalysis, their high cost and potential cyclic degradation urgently require the development of alternatives [5,6]. Palladium, with its analogous face-centered cubic structure and higher crustal abundance, has emerged as a rational alternative to Pt [7,8]. Nevertheless, intrinsic limitations persist: monometallic Pd exhibits suboptimal oxygen binding energies due to its elevated d-band center position, leading to excessive adsorption of reaction intermediates (*OOH, *O)[1] [9–11].

Recent advances demonstrate that alloying Pd with transition metals (e.g., Fe, Co, Ni) can engineer the electronic structure through strain and ligand effects, thereby optimizing intermediate adsorption-desorption kinetics [12–14]. For instance, Luo et al. synthesized ultra-thin Pd–Mo alloy nanosheets with sub-nanometer thickness, where the alloying effect modulated the electronic structure of the system, optimizing oxygen binding and enabling exceptionally efficient and stable ORR electrocatalytic performance [15]. Sahoo et al. synthesized ultra-thin twisted PdNi alloy nanowires (NWs), in which the incorporation of Ni fine-tuned the Pd d-band center, enhancing ORR efficiency and facilitating the continuous regeneration of active site [16]. However, the key challenge remains to achieve uniformity in alloy formation while suppressing phase separation—a common problem when using inorganic metal salts such as $FeCl_3$, which creates harmful halide residues [17,18]. Here, we address these limitations by selecting metal phthalocyanine precursors and ultra-fast heat treatment.

Iron phthalocyanine (FePc) represents an ideal molecular precursor for alloy synthesis, offering three synergistic advantages: (1) The macrocyclic ligand acts as an intrinsic N-donor, enabling in situ formation of conductive N-doped carbon matrices during pyrolysis, which facilitates electron transfer via Pd–N–C coordination; (2) Controlled thermal decomposition of FePc ensures atomic dispersion of Fe species, favoring homogeneous PdFe alloy nucleation over iron oxide formation; (3) Unlike chloride-containing precursors, FePc eliminates detrimental halide incorporation, which otherwise passivates active sites through competitive adsorption [19–22]. Complementing this precursor strategy, cetyltrimethylammonium bromide (CTAB) plays an indispensable

---

[*] Corresponding author.

[**] Corresponding author.

E-mail addresses: wudanyang@dlmu.edu.cn (D. Wu), bjchen@dlmu.edu.cn (B. Chen).

[1] *OOH and *O signify species adsorbed on the catalyst surface. Specifically: *OOH represents the adsorbed hydroperoxyl intermediate, *O represents the adsorbed atomic oxygen intermediate.

https://doi.org/10.1016/j.ijhydene.2025.05.400
Received 5 April 2025; Received in revised form 27 May 2025; Accepted 29 May 2025

templating role. Its amphiphilic structure guides the self-assembly of Pd/Fe precursors on carbon support, limiting the growth of nanoparticles to sizes below 10 nm while preventing agglomeration during rapid thermal processing [23–25].

Hererin, we employ advanced Joule heating, which provides ultrafast thermal shock to dynamically capture metastable alloy phases, while avoiding nanoparticle coalescence through quenching rates. This approach uniquely preserves the structural synergies derived from FePc and CTAB, yielding a catalyst where well-dispersed PdFe nanoparticles (~9.9 nm average size) are anchored on a hierarchical N-doped carbon framework (542 m^2/g surface area). The resultant NC-FePd catalyst achieves an exceptional half-wave potential in alkaline media, outperforming Pt/C while demonstrating negligible decay after 5000 cycles. Our work establishes a universal strategy for synthesizing high-performance alloy catalysts by synergizing molecular precursor design, surfactant-mediated morphology control, and ultra-fast thermal processing.

2. Experimental

2.1. Chemicals

Iron (II) Phthalocyanine ($C_{32}H_{16}FeN_8$, ≥98 %), Palladium (II) acetylacetonate (Pd $(acac)_2$, 99 %), Cetyltrimethylammonium bromide ($C_{19}H_{42}BrN$, ≥98 %), Potassium hydroxide (KOH, 99.999 %) and Nafion solution (5 wt%, Sigma-Aldrich) were ordered from Aladdin. Carbon black (ECP600JD) was ordered from Zhongke Youxuan (Beijing) Holding Group Co., Ltd. Ethanol (C_2H_6O, 99.9 %) was ordered from Titan Scientific Co., Ltd. All reagents utilized needed no further purification.

2.2. Synthesis of NC-FePd catalyst

The NC-FePd was synthesized through a rapid high-temperature heating process (see Fig. 1). Firstly, 0.2 mmol Pd $(acac)_2$, 0.1 mmol Iron (II) Phthalocyanine, 50 mg CTAB and 100 mg carbon black was added to 30 mL ethanol. The solution was ultrasonicated for 30 min and stirred overnight to obtain a uniformly dispersed black suspension. After centrifugation and drying, the dry black fine powder is collected and loaded with carbon paper for further pyrolysis treatment. The process is pyrolyzed to 1000 °C in 0.5 s by Joule heating under the protection of Ar atmosphere and cooled rapidly within 5 s, resulting in a product named NC-FePd. It is collected and fully ground for further testing. To compare the impact of incorporating iron phthalocyanine on the catalytic performance, a comparison sample was prepared. The preparation method was the same as that of NC-FePd, but the difference was that no iron phthalocyanine was added in the precursor preparation, and the sample was named NC-Pd. To further verify the unique advantages of the Joule-heating and the nitrogen-doped carbon framework, the N-free PdFe/carbon composite denoted as C–PdFe was prepared using the same Joule-heating process as NC-PdFe, but removing the N source from the precursor and replacing Iron (II) Phthalocyanine with Iron (III) chloride hexahydrate. The PdFe/carbon composite prepared via a traditional tube furnace calcination method using the same precursor preparation process as NC-PdFe was denoted as Conventional PdFe/C.

3. Results and discussion

3.1. Structural characterization

Scanning electron microscopy (SEM) was employed to conduct a morphological characterization of NC-FePd. Fig. 2a and b clearly demonstrate the three-dimensional porous architecture formed by interconnected FePd nanoparticle assemblies anchored on the N-doped carbon architecture. Transmission electron microscopy (TEM) analysis in Fig. 2c and Fig. S1 again reveals homogeneous dispersion of well-defined metallic nanoparticles on the carbon substrate, with statistical particle size analysis (inset) yielding a narrow distribution centered at 9.9 ± 1.2 nm. This spatial uniformity and nanoscale dimensionality are critical for maximizing accessible active sites, thereby promoting electrocatalytic efficiency [26,27]. The high-resolution TEM (HR-TEM) analysis reveals well-defined lattice spacings of 0.223 nm, which align with (111) planes of the face-centered cubic (fcc) $FePd_3$ phase, confirming the successful formation of carbon-supported $FePd_3$ alloy nanoparticles (Fig. 2d) [28]. The energy dispersive X-ray spectroscopy (EDX) analysis was employed to examine the element distribution within the NC-FePd catalyst. In Fig. 2e–j, the elements of C, N, O, Pd, and Fe are evenly dispersed within the NC-FePd alloy catalyst. Furthermore, the overlapping spatial profiles of Fe and Pd signals demonstrate

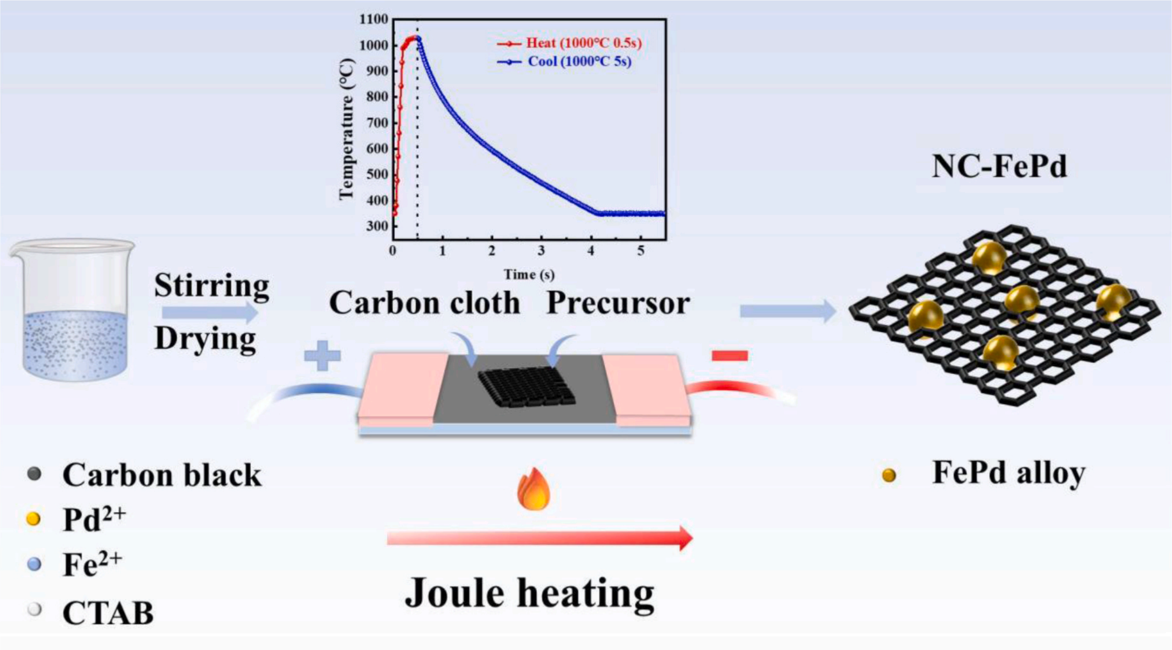

Fig. 1. Schematic diagram illustrating the Joule heating method for the synthesis of the NC-FePd catalyst.

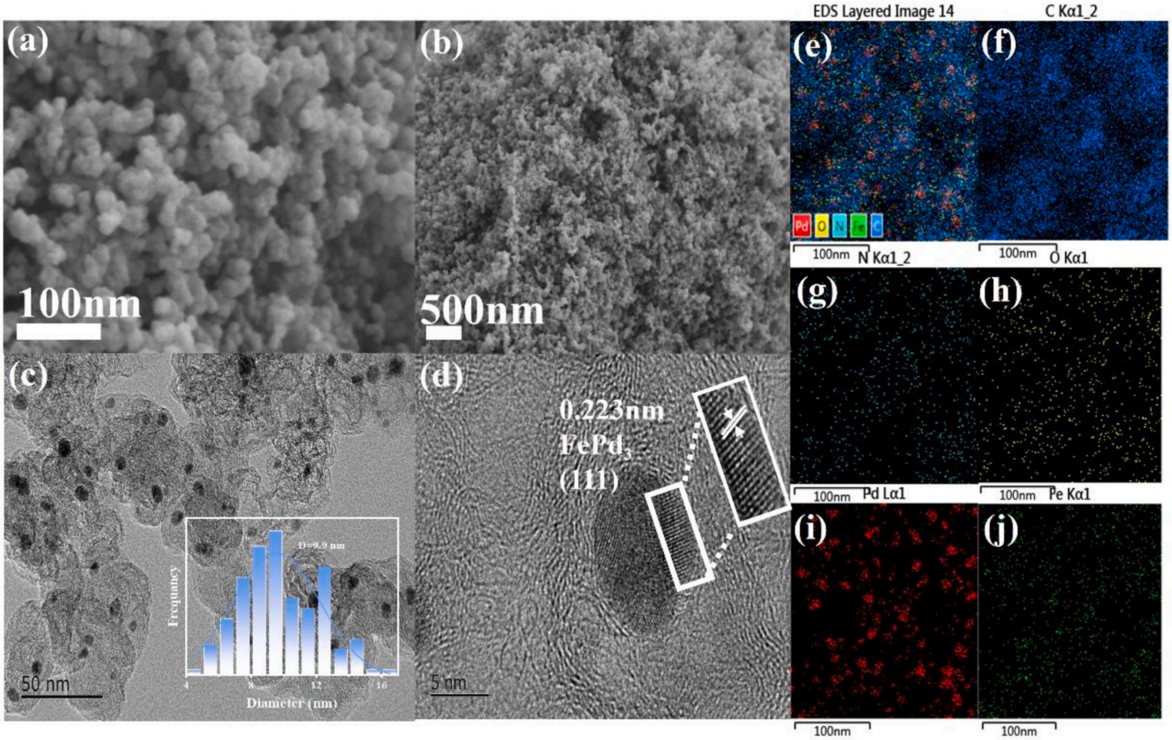

Fig. 2. (a–b) SEM, (c) TEM, (d) HR-TEM, (e–j) Elemental mapping of NC-FePd (C, N, O, Pd, Fe).

atomic-level mixing of both metallic components, verifying the alloyed structure rather than core-shell or phase-segregated configurations [29, 33]. The EDS maps confirm the absence of segregated Pd-rich or Fe-rich domains, instead revealing a seamless distribution of both elements, indicative of their incorporation into a single Fe–Pd alloy lattice. This atomic-scale mixing is essential for enabling strong metal-metal interactions, which modulate the electronic environment of active sites and enhance ORR performance. Meanwhile, the homogeneous incorporation of nitrogen within the carbon framework (Fig. 2g) originates from the introduction of iron phthalocyanine as an iron source, which serves as both structural scaffold and electronic modifier through formed Pd–N–C coordination bonds [30,31].

These microscopic observations correlate well with the X-ray diffraction (XRD) data (Fig. 3a), where the characteristic peaks shift systematically relative to pure Pd, confirming lattice parameter alterations induced by Fe alloying. As depicted in Fig. 3a, two characteristic

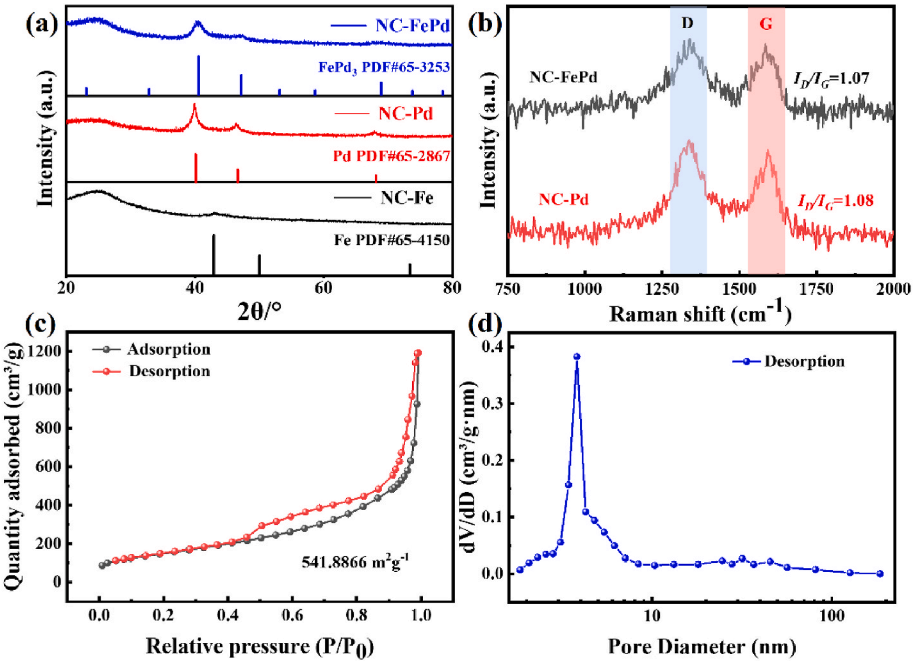

Fig. 3. (a) The XRD patterns of NC-FePd, NC-Pd, and NC-Fe, (b) the Raman spectra of NC-FePd and NC-Pd, (c) N_2 adsorption-desorption isotherms of NC-FePd, (d) Pore size distribution curve of NC-FePd.

peaks at 40.501° (111) and 47.114° (210) align precisely with the face-centered cubic (fcc) phase of FePd$_3$, excluding the presence of metallic Fe or Pd secondary phases [32,33]. The synergetic combination of phase-pure FePd$_3$ nanocrystals and nitrogen-enriched conductive support establishes an optimized electron transfer network, which is pivotal for achieving enhanced catalytic kinetics as demonstrated in subsequent electrochemical tests. Meanwhile, the NC-Fe clearly exhibits only Fe-related characteristic peaks at 42.9° (111), 49.9° (200), and 73.3° (220) corresponding to metallic Fe (PDF# 65–4150). The absence of Pd signals in NC-Fe validates the unique formation of FePd$_3$ alloy structures in NC-FePd, which are critical for enhancing ORR activity through synergistic interactions. Raman spectral analysis (Fig. 3b) reveals fundamental carbon structural evolution. The intensity ratio (I_D/I_G) derived from D-band (1350 cm^{-1}) and G-band (1580 cm^{-1}) was 1.07, suggesting a slight increase in graphitization when alloyed with Fe, compared to NC-Pd ($I_D/I_G = 1.08$). This improved structural integrity facilitates electron delocalization through sp^2-conjugated networks [34,35]. However, this difference alone cannot definitively prove the occurrence of graphitization. Subsequently, the textural properties of NC-FePd, including specific surface area and pore characteristics, were analyzed using N$_2$ adsorption-desorption measurements. Fig. 3c reveals that NC-FePd exhibits a BET surface area of 541.9 m^{2}g^{-1}, while its total pore volume reaches 1.8 cm^3 g^{-1}. The typical type-IV isotherm hysteresis loop coupled with the corresponding pore distribution in Fig. 4d confirms the coexistence of abundant mesopores and micropores. Such architectured porosity not only maximizes metal nanoparticle dispersion but also ensures rapid O$_2$ diffusion kinetics during ORR [36–38].

The chemical states and electronic interaction within the PdFe alloy were systematically elucidated through high-resolution X-ray photoelectron spectroscopy (XPS). The full-scale spectrum (Fig. S2) corroborating that C, N, O, Pd, and Fe are present in NC-FePd. In Fig. 4a, the Pd 3d spectrum can be separated into two sets of doublet peaks, with the Pd 3d peaks at 335.76 eV and 341.18 eV corresponding to metallic Pd (Pd^0) 3d$_{5/2}$ and 3d$_{3/2}$, respectively. Two peaks observed at 336.85 eV and 342.76 eV suggest that there exist trace amounts of Pd^{2+}, which are likely originating from surface-oxidized PdO or Pd(OH)$_2$ [39–41]. Notably, compared to NC-Pd, the Pd 3d peaks in NC-FePd exhibit a positive shift of 0.2 eV, confirming the strong electron interaction within NC-FePd. The observed binding energy shift suggests charge redistribution between Pd and Fe atoms, leading to significant electronic modification of the Pd species, thus improving the adsorption energy of intermediates in catalytic reactions and boosting catalytic performance [42]. The Fe 2p spectrum (Fig. 4b) demonstrates mixed oxidation states: the characteristic doublet at 707.91 eV (2p$_{3/2}$) and 720.69 eV (2p$_{1/2}$) confirms metallic Fe^0 domains, whereas doublet at 711.02 eV and 724.51 eV corresponds to Fe^{2+} species, probably forming passivating oxide layers during pyrolysis [44,45]. The N 1s spectrum in Fig. 4c displays three deconvoluted peaks at 398.97 eV, 400.12 eV, and 401.39 eV corresponding to pyridinic N, pyrrolic N, and graphitic N, respectively. Among these configurations, the abundant pyridinic N is particularly advantageous, as these edge-site N atoms enhance metal-support interactions and provide active sites for oxygen adsorption [46]. In NC-FePd, the pyridinic N content is significantly higher than that in NC-Pd (Fig. S3a). This increase in pyridinic N species indicates that Fe–Pd alloying promotes the formation of active nitrogen sites, which are critical for O$_2$ adsorption and ORR kinetics. In the C 1s spectrum (Fig. 4d), hybrid carbon peaks associated with C–N, C═N, and C═C are observed at 288.61 eV, 285.60 eV, and 284.83 eV, respectively. The abundance of C═C bonds strongly correlate with the graphitization level in catalyst [47]. The C–N bond peak in NC-FePd lower than in NC-Pd (285.6 eV) (Fig. S3b). This downshift in binding energy confirms that Fe–Pd alloying induces electron transfer from Fe to the C–N bond, creating a more electron-rich carbon environment. This electronic enrichment facilitates stronger O$_2$ adsorption and faster activation at the active sites. Inductively coupled plasma optical emission spectroscopy (ICP-OES) quantitatively revealed a Pd/Fe atomic ratio of 3.1 in the synthesized NC-FePd catalyst, exhibiting excellent agreement with the theoretically designed stoichiometric ratio for the PdFe alloy phase.

3.2. Electrochemical performance

The catalytic performance of synthesized NC-FePd is able to be

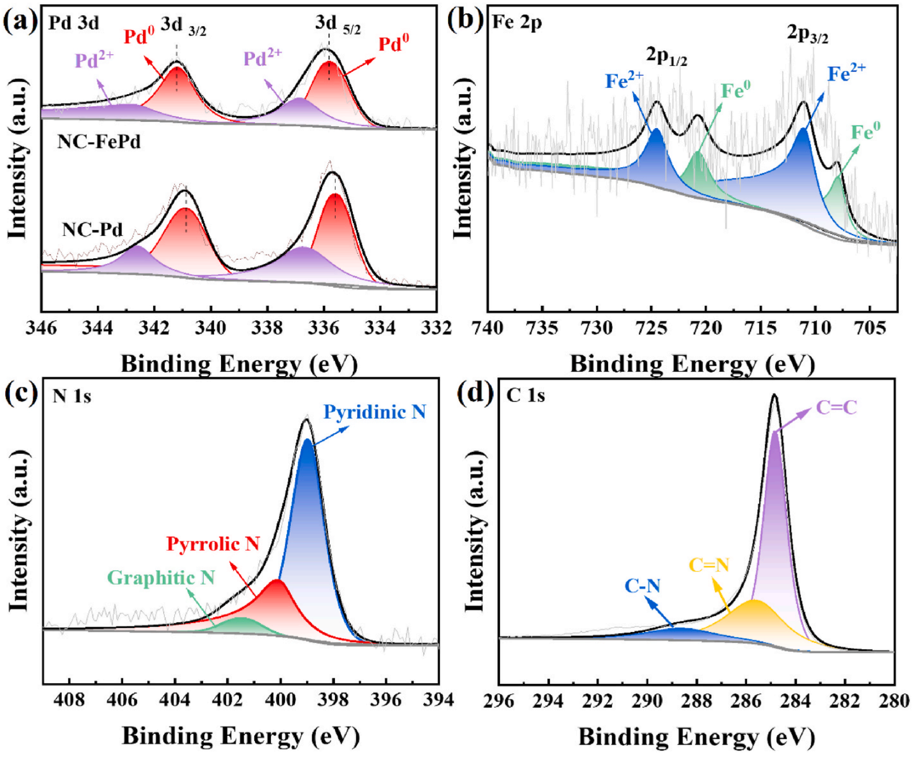

Fig. 4. (a) Pd 3d XPS spectra of NC-FePd and NC-Pd, (b) Fe 2p, (c) N 1s, and (d) C 1s spectra of NC-FePd.

thoroughly assessed using a variety of characterization techniques. Initially, the cyclic voltammetry (CV) curve in Fig. 5a reveals that the cathodic reduction peak of NC-FePd (0.89 V vs. RHE) in O_2-saturated environment is notably enhanced by 140 mV compared to that of NC-Pd (0.75 V vs. RHE). Moreover, the absence of peaks in both samples under an N_2-saturated environment confirms that NC-FePd exhibits a distinct response to the oxygen reduction reaction, outperforming NC-Pd. This is attributed to the fact that Pd, with its strong adsorption for oxygen species, tends to hinder their desorption, thereby reducing catalytic activity. However, alloying Pd with Fe weakens the Pd–O bond, which theoretically enhances ORR performance. Subsequently, linear sweep voltammetry (LSV) by rotating disk electrode (RDE) was employed to further assess the ORR activity of NC-FePd and NC-Pd. As illustrated in the polarization curve (Fig. 5b), NC-FePd exhibits exceptional ORR catalytic activity, with a half-wave potential ($E_{1/2}$) of 0.84 V vs. RHE, representing 20 mV positive shift in comparison with Pt/C (0.82 V vs. RHE). Meanwhile, C–PdFe exhibited significantly reduced activity, with a $E_{1/2}$ of 0.749 V vs. RHE. The Conventional PdFe/C also showed suboptimal performance, with a $E_{1/2}$ of 0.774 V vs. RHE (Fig. S4). These results demonstrate that N-doping and Joule-heating method are critical for enhancing catalyst activity, underscoring the irreplaceable role of our synthetic strategy. Additionally, its limiting current density (J_L) reaches 6.01 mA cm^{-2}, surpassing the value of Pt/C (5.67 mA cm^{-2}). Notably, NC-PdFe exhibits a higher J_L consistent with the O_2 diffusion-limited regime where J_L is governed by mass transfer (controlled by the rotation rate) rather than intrinsic catalytic activity. These results further validate that integrating PdFe alloy into carbon supports significantly enhances electrocatalytic performance. Furthermore, Fig. 5c presents the Tafel plot derived from the LSV curve in the low overpotential region, revealing that NC-FePd exhibits the lowest Tafel slope of 53.73 mV dec^{-1}, compared to NC-Pd (102.02 mV dec^{-1}) and commercial Pt/C (91.32 mV dec^{-1}). These results demonstrate that NC-FePd possesses significantly faster reaction kinetics. By recording the polarization curves across rotational speeds at 400–2500 rpm (Fig. 5d), it turns out that J_L rises with ascending rotational speeds, as the accelerated ion transfer rate on the electrode surface enhances the reaction kinetics. The electron transfer number (n) can be computed using Koutecky-Levich (K-L) graphs taken at various potentials, which are obtained from rotation speed-dependent measurements (see inset in Fig. 5d). The fitted lines at each potential are parallel, with the average electron transfer number (n) approaching the theoretical value of 4, aligning well with the fitted data [48,49]. This consistency suggests a dominant four-electron transfer mechanism during ORR. Subsequently, the rotating ring disk electrode (RRDE) experiment of NC-FePd was performed (Fig. 5e) to precisely evaluate n and H_2O_2 yield (% H_2O_2). The NC-FePd exhibits an H_2O_2 yield under 5 % within the voltage interval between 0.2 V and 0.8 V (Fig. 5f), corresponding to an n value close to 4. These results are consistent with the RDE findings, reaffirming that NC-FePd operates via a four-electron transfer pathway [50].

To evaluate the durability of NC-FePd, it was continuously cycled in electrolyte. After 5000 CV cycles, NC-FePd exhibited minimal attenuation in its $E_{1/2}$, with only a 2 mV negligible negative shift (Fig. 6a), demonstrating exceptional durability in ORR under alkaline conditions. The slight reduction of the limiting current density is likely due to an inevitable detachment of catalyst from the electrode surface in the test [51]. Additionally, methanol tolerance is also a crucial factor in determining the practical effectiveness of catalysts [52,53]. Thus, the ORR polarization curves of NC-FePd were compared before and after the injection of a specific amount of methanol (Fig. 6b). The results revealed almost no degradation in catalytic activity. NC-FePd exhibits outstanding electrocatalytic activity and exceptional methanol tolerance. It effectively mitigates the adverse effects of methanol crossover between electrodes, demonstrating its great potential as a cathode catalyst in fuel cell technology.

4. Conclusions

The rapid Joule heating synthesis strategy presented in this work enables the precise fabrication of nitrogen-carbon-supported cubic-phase $FePd_3$ nanoparticles with tailored electronic properties and enhanced catalytic functionality. By leveraging ultrafast thermal cycling (1000 °C in 0.5 s), the $FePd_3$ alloy achieves uniform dispersion and minimized agglomeration, with Fe doping inducing lattice expansion and electron redistribution as evidenced by XRD and XPS. The hierarchical porous carbon support stabilizes the $FePd_3$ nanoparticles through strong metal-carrier interactions, while nitrogen doping optimizes

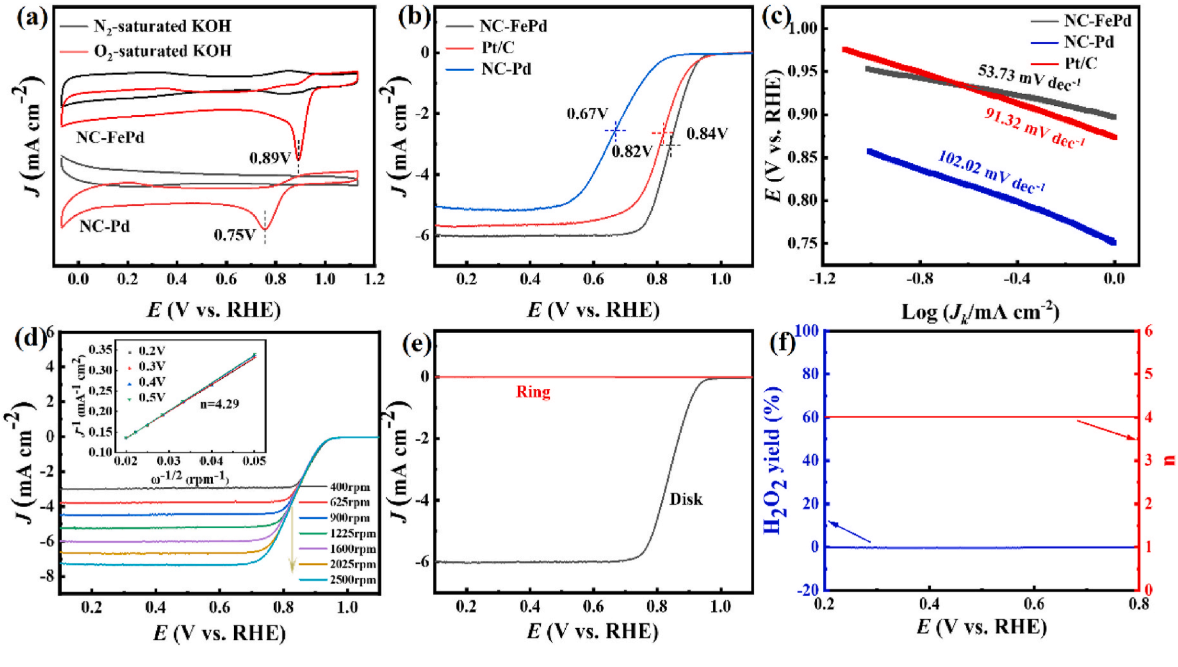

Fig. 5. (a) CV profiles of NC-FePd and NC-Pd, (b) ORR polarization curves of NC-FePd, NC-Pd, and Pt/C, (c) Tafel slopes of NC-FePd, NC-Pd, and Pt/C, (d) ORR polarization curves of NC-FePd at varying rotation rates, (Insert: *K-L* plots and n), (e) LSV profile of NC-FePd recorded via an RRDE, (f) H_2O_2 yield and n derived from RRDE measurements.

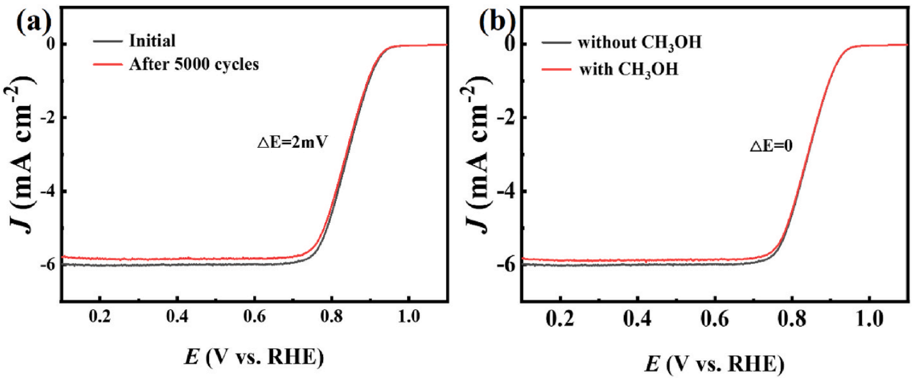

Fig. 6. (a) Durability test for NC-FePd in an O_2-saturated 0.1 M KOH solution, (b) Methanol toxicity resistance test for NC-FePd in an O_2-saturated 0.1 M KOH solution.

surface reactivity and charge transfer, contributing to exceptional durability and methanol resistance during prolonged cycling. The scalability of this synthesis method highlights its potential for designing other multi-component Pd-based alloys (e.g., PdNi, PdCo) with controlled phase structures and catalytic-enhanced properties.

CRediT authorship contribution statement

Dandan Jiang: Formal analysis, Data curation. **Danyang Wu:** Writing – review & editing, Conceptualization. **Yu Wang:** Investigation. **Yongze Cao:** Software. **Xizhen Zhang:** Methodology. **Baojiu Chen:** Project administration.

Declaration of competing interest

The authors declare that they have no known competing financial interests or personal relationships that could have appeared to influence the work reported in this paper.

Acknowledgments

This work was financially supported by the Fundamental Research Funds for the Central Universities (Grant Nos. 3132023519 & 3132024188).

Appendix A. Supplementary data

Supplementary data to this article can be found online at https://doi.org/10.1016/j.ijhydene.2025.05.400.

References

[1] Tao J, Wang X, Xu M, Liu C, Ge J, Xing W. Non-noble metals as activity sites for ORR catalysts in proton exchange membrane fuel cells (PEMFCs). Ind Chem Mater 2023;1:388–409.

[2] Li Y, Zhang P, Wan L, Zheng Y, Qu X, Zhang H, Wang Y, Zaghib K, Yuan J, Sun S, Wang Y, Zhou Z, Sun S. A general carboxylate-assisted approach to boost the ORR performance of ZIF-derived Fe/N/C catalysts for proton exchange membrane fuel cells. Adv Funct Mater 2021;31:2009645.

[3] Qi W, Huang W, Niu J, Zhang B, Zhang Z, Li W. The role of S in the Co-N-S-C catalysis system towards the ORR for proton exchange membrane fuel cells. Appl Surf Sci 2021;540:148325.

[4] Wang R, Zhang P, Wang Y, Wang Y, Zaghib K, Zhou Z. ZIF-derived Co-N-C ORR catalyst with high performance in proton exchange membrane fuel cells. Prog Nat Sci Mater 2020;30:855–60.

[5] Jiang H, Xia J, Jiao L, Meng X, Wang P, Lee C, Zhang W. Ni single atoms anchored on N-doped carbon nanosheets as bifunctional electrocatalysts for Urea-assisted rechargeable Zn-air batteries. Appl Catal B Environ 2022;310:121352.

[6] Ding R, Liu Y, Rui Z, Li J, Liu J, Zou Z. Facile grafting strategy synthesis of single-atom electrocatalyst with enhanced ORR performance. Nano Res 2020;13:1519–26.

[7] Zeng T, Meng X, Sun S, Ling M, Zhang C, Yuan W, Cao D, Niu M, Zhang L, Li C. Tensile-strained holey Pd metallene toward efficient and stable electrocatalysis. Small Methods 2023;7:2300791.

[8] Guo J, Jiao S, Ya X, Zheng H, Wang R, Yu J, Wang H, Zhang Z, Liu W, He C, Fu X. Ultrathin Pd-based perforated nanosheets for fuel cells electrocatalysis. Chemelectrochem 2022;9:e202200729.

[9] Zhang F, Sun S, Ge X, Guan Q, Ling M, Yuan W, Zhang L. Synthesizing Pd-based high entropy alloy nanoclusters for enhanced oxygen reduction. Chem Commun 2024;60:3591–4.

[10] Zhang J, Xu W, Liu Y, Hung S, Liu W, Lam Z, Tao H, Yang H, Cai W, Xiao H, Chen H, Liu B. In situ precise tuning of bimetallic electronic effect for boosting oxygen reduction catalysis. Nano Lett 2021;21:7753.

[11] Zhuang S, Chen D, You Q, Fan W, Yang J, Wu Z. Thiolated, reduced palladium nanoclusters with resolved structures for the electrocatalytic reduction of oxygen. Angew Chem Int Ed 2022;61:e202208751.

[12] Li Q, Sun C, Sun X, Yin Z, Du Y, Liu J, Luo F. Synthesis of palladium-rare earth alloy as a high-performance bifunctional catalyst for direct ethanol fuel cells. Nano Res 2024;17:9525–31.

[13] Qiao S, Shou H, Xu W, Cao Y, Zhou Y, Wang Z, Wu X, He Q, Song L. Regulating and identifying the structures of PdAu alloys with splendid oxygen reduction activity for rechargeable zinc-air batteries. Energy Environ Sci 2023;16:5842–51.

[14] Zhang W, Chang J, Wang G, Li Z, Wang M, Zhu Y, Li B, Zhou H, Wang G, Gu M, Feng Z, Yang Y. Surface oxygenation induced strong interaction between Pd catalyst and functional support for zinc-air batteries. Energy Environ Sci 2022;15:1573–84.

[15] Luo M, Zhao Z, Zhang Y, Sun Y, Xing Y, Lv F, Yang Y, Zhang X, Hwang S, Qin Y, Ma J, Lin F, Sun D, Lu G, Guo S. PdMo bimetallene for oxygen reduction catalysis. Nature 2019;574:81–5.

[16] Sahoo L, Garg R, Kaur K, Vinod C, Gautam U. Ultrathin twisty PdNi alloy nanowires as highly active ORR electrocatalysts exhibiting morphology-induced durability over 200 K cycles. Nano Lett 2022;22:246–54.

[17] Chen Y, Choi Y, Yoo S, Ding Y, Yan R, Pei K, Qu C, Zhang L, Chang I, Zhao B, Zhang Y, Chen H, Chen Y, Yang C, DeGlee B, Murphy R, Liu J, Liu M. A highly efficient multi-phase catalyst dramatically enhances the rate of oxygen reduction. Joule 2018;2:938–49.

[18] Ciszek K, Pacześniak T, Zaborniak I, Bloniarz P, Surmacz K, Sobkowiak A, Chmielarz P. Iron-based catalytically active complexes in preparation of. Funct. Mater. Process. 2020;8:1683.

[19] Chen K, Liu K, An P, Li H, Lin Y, Hu J, Jia C, Fu J, Li H, Liu H, Lin Z, Li W, Li J, Lu Y, Chan T, Zhang N, Liu M. Iron phthalocyanine with coordination induced electronic localization to boost oxygen reduction reaction. Nat Commun 2020;11:4173.

[20] Zhang Z, Dou M, Ji J, Wang F. Phthalocyanine tethered iron phthalocyanine on graphitized carbon black as superior electrocatalyst for oxygen reduction reaction. Nano Energy 2017;34:338–43.

[21] Yang J, Tao J, Isomura T, Yanagi H, Moriguchi I, Nakashima N. A comparative study of iron phthalocyanine electrocatalysts supported on different nanocarbons for oxygen reduction reaction. Carbon 2019;145:565–71.

[22] Mei Z, Cai S, Zhao G, Zou X, Fu Y, Jiang J, An Q, Li M, Liu T, Guo H. Boosting the ORR active and Zn-air battery performance through ameliorating the coordination environment of iron phthalocyanine. Chem Eng J 2022;430:132691.

[23] Fan C, Li G, Gu J, Wang Q, Li S, Li B. Molten-salt electrochemical deoxidation synthesis of platinum-neodymium nanoalloy catalysts for oxygen reduction reaction. Small (Weinh) 2023;19:2300110.

[24] Li Y, Wang F, Zhu H. Synthesis of H_2O_2-CTAB dual-modified carbon black-supported Pt_3Ni to improve catalytic activity for ORR. J Mater Sci 2020;55:11241–52.

[25] Parkash A. CTAB-capped copper nanoparticles coated on N doped carbon layer and encapsulated in ZIF-67: a highly-efficient ORR catalyst. J Porous Mater 2020;27:1377–87.

[26] Xiong X, Tang J, Ji Y, Xue W, Wang H, Liu C, Zeng H, Dai Y, Peng H, Zheng T, Xia C, Liu X, Jiang Q. High-efficiency iridium-yttrium alloy catalyst for acidic water electrolysis. Adv Energy Mater 2024;14:2304479.

[27] Jiang N, Wang H, Jin H, Liu X, Guan L. Embedding the intermetallic Pt_5Ce alloy in mesopores through Pt-C coordination layer interactions as a stable electrocatalyst for the oxygen reduction reaction. EES Catal 2024;2:1253–62.

[28] Yin H, Liu S, Zhang C, Bao J, Zheng Y, Han M, Dai Z. Well-coupled graphene and Pd-based bimetallic nanocrystals nanocomposites for electrocatalytic oxygen reduction reaction. ACS Appl Mater Interfaces 2014;6:2086–94.

[29] Lin F, Li M, Zeng L, Luo M, Guo S. Intermetallic nanocrystals for fuel-cells-based electrocatalysis. Chem Rev 2023;123:12507–93.

[30] Hong Y, Li L, Huang B, Tang X, Zhai W, Hu T, Yuan K, Chen Y. Molecular control of carbon-based oxygen reduction electrocatalysts through metal macrocyclic complexes functionalization. Adv Energy Mater 2021;11:2100866.

[31] Peng Y, Li Z, Xia D, Zheng L, Liao Y, Li K, Zuo X. Probing the influence of the center atom coordination structure in iron phthalocyanine multi-walled carbon nanotube-based oxygen reduction reaction catalysts by X-ray absorption fine structure spectroscopy. J Power Sources 2015;291:20–8.

[32] Fan Z, Zhang H. Crystal phase-controlled synthesis, properties and applications of noble metal nanomaterials. Chem Soc Rev 2016;45:63–82.

[33] Ramanathan M, Ramani V, Prakash J. Kinetics of the oxygen reduction reaction on Pd_3M (M = Cu, Ni, Fe) electrocatalysts synthesized at elevated annealing temperatures. Electrochim Acta 2012;75:254–61.

[34] Yang Y, Huang H, Shen B, Jin L, Jiang Q, Yang L, He H. Anchoring nanosized Pd on three-dimensional boron- and nitrogen-codoped graphene aerogels as a highly active multifunctional electrocatalyst for formic acid and methanol oxidation reactions. Inorg Chem Front 2020;7:700–8.

[35] Tatarova E, Dias A, Henriques J, Botelho do Rego A, Ferraria A, Abrashev M, Luhrs C, Phillips J, Dias F, Ferreira C. Microwave plasmas applied for the synthesis of free standing graphene sheets. J Phys D Appl Phys 2014;47:385501.

[36] Hong P, Zhang K, He J, Li Y, Wu Z, Xie C, Liu J, Kong L. Selenization governs the intrinsic activity of copper-cobalt complexes for enhanced non-radical Fenton-like oxidation toward organic contaminants. J Hazard Mater 2022;435:128958.

[37] Zhao Y, Wen J, Li P, Zhang P, Wang S, Li D, Dou J, Li Y, Ma H, Xu LA. "Pre-Division metal clusters" strategy to mediate efficient dual-active sites ORR catalyst for ultralong rechargeable Zn-air battery. Angew Chem Int Ed 2023;62:e202216950.

[38] Kim H, Yang H, Kang J, Takeuchi N. Multifunctional disordered sulfur-doped carbon for efficient sodium-ion-exchange and 2-electron-transfer-dominant oxygen reduction reaction. Carbon 2021;182:242–53.

[39] Zheng M, Wang P, Zhi X, Yang K, Jiao Y, Duan J, Zheng Y, Qiao S. Electrocatalytic CO_2-to-C_{2+} with ampere-level current on heteroatom-engineered copper via tuning *CO intermediate coverage. J Am Chem Soc 2022;144:14936–44.

[40] Tressaud A, Khairoun S, Touhara H, Watanabe N. X-ray photoelectron spectroscopy of palladium fluorides. Z Anorg Allg Chem 1986;540:291–9.

[41] Thi M, Tran T, Anh P, Nhac-Vu H, Bui Q. An innovative catalyst of nickel-palladium alloy nanocrystals embedded nitrogen-doped graphene for efficient oxygen reduction reaction. J Alloys Compd 2019;797:314–24.

[42] Martins M, Šljukić B, Metin Ö, Sevim M, Sequeira C, Sener T, Santos D. Bimetallic PdM (M= Fe, Ag, Au) alloy nanoparticles assembled on reduced graphene oxide as catalysts for direct borohydride fuel cells. J Alloys Compd 2017;718:204–14.

[44] Zhu S, Ding L, Zhang X, Wang K, Wang X, Yang F, Han G. Biaxially-strained phthalocyanine at Polyoxometalate@Carbon nanotube heterostructure boosts oxygen reduction catalysis. Angew Chem 2023;135:e202309545.

[45] Sheng X, Mei Z, Jing Q, Zhou X, Wang L, Xu Q, Yang L, Guo H. Cross-linked double-active centers for efficient pH-universal oxygen reduction catalysis. ACS Sustainable Chem Eng 2023;11:7263.

[46] Fei H, Dong J, Arellano-Jiménez M, Ye G, Kim N, Samuel E, Peng Z, Zhu Z, Qin F, Bao J, Yacaman M, Ajayan P, Chen D, Tour J. Atomic cobalt on nitrogen-doped graphene for hydrogen generation. Nat Commun 2015;8668:1–8.

[47] Fan C, Wang X, Wu X, Chen Y, Wang Z, Li M, Sun D, Tang Y, Fu G. Neodymium-evoked valence electronic modulation to balance reversible oxygen electrocatalysis. Adv Energy Mater 2023;13:2203244.

[48] Zeng H, Wang W, Li J, Luo J, Chen S. In situ generated dual-template method for Fe/N/S Co-doped hierarchically porous honeycomb carbon for high-performance oxygen reduction. ACS Appl Mater Interfaces 2018;10:8721–9.

[49] Woo J, Lim J, Kim J, Joo S. Heteroatom-doped carbon-based oxygen reduction electrocatalysts with tailored four-electron and two-electron selectivity. Chem Commun 2021;57:7350–61.

[50] Lu F, Zhang Y, Liu S, Lu D, Su D, Liu M, Zhang Y, Liu P, Wang J, Adzic R, Gang O. Surface proton transfer promotes four-electron oxygen reduction on gold nanocrystal surfaces in alkaline solution. J Am Chem Soc 2017;139:7310–7.

[51] Koh S, Toney M, Strasser P. Activity-stability relationships of ordered and disordered alloy phases of Pt_3Co electrocatalysts for the oxygen reduction reaction (ORR). Electrochim Acta 2007;52:2765–74.

[52] Antolini E, Lopes T, Gonzalez E. An overview of platinum-based catalysts as methanol-resistant oxygen reduction materials for direct methanol fuel cells. J Alloys Compd 2008;461:253–62.

[53] Shi Q, He Y, Bai X, Wang M, Cullen D, Lucero M, Zhao X, More K, Zhou H, Feng Z, Liu Y, Wu G. Methanol tolerance of atomically dispersed single metal site catalysts: mechanistic understanding and high-performance direct methanol fuel cells. Energy Environ Sci 2020;13:3544–55.